Optical and Quantum Electronics (2020) 52:89
https://doi.org/10.1007/s11082-020-2225-x

# Numerical modeling of photonic crystal semiconductor optical amplifiers-based 160 Gb/s all-optical NOR and XNOR logic gates

**Amer Kotb**[1,2] · **Chunlei Guo**[1,3]

Received: 18 September 2019 / Accepted: 23 January 2020 / Published online: 29 January 2020


**Abstract**
A photonic crystal (PC) is a periodic optical nanostructure typically containing ordered arrays of holes that confine and control the motion of photons. Moreover, PC strongly modifies the dispersion relationship. The conventional semiconductor optical amplifier (SOA), on the other hand, is an attractive nonlinear element due to its strong nonlinearity, compactness, power efficiency, and integration potential with other optoelectronic devices. Thus, we combine the unique features of PC with those of SOA to numerically model ultrafast all-optical NOT-OR (NOR) and exclusive-NOR (XNOR) logic gates at 160 Gb/s. A comparison is made between PCSOAs and conventional SOAs schemes through examining the variation of the quality factor (QF) against the key operational parameters, including the effects of the amplified spontaneous emission and operating temperature, in order to obtain more realistic results. The obtained results confirm that the considered logic operations using PCSOAs are capable of operating at 160 Gb/s with higher QF than when having conventional SOAs.

**Keywords** All-optical NOR logic gate · All-optical XNOR logic gate · Photonic crystal semiconductor optical amplifier · Mach–Zehnder interferometer · Quality factor

## 1 Introduction

Conventional semiconductor optical amplifiers (SOAs) have recently attracted a huge number of interests as nonlinear elements due to their strong nonlinearity, compact size, power efficiency, low cost, and integration potential with other optoelectronic devices over all

✉ Amer Kotb
amer@ciomp.ac.cn

✉ Chunlei Guo
guo@optics.rochester.edu

[1] The Guo Photonics Laboratory, Changchun Institute of Optics, Fine Mechanics, and Physics, Chinese Academy of Sciences, Changchun 130033, China

[2] Department of Physics, Faculty of Science, University of Fayoum, Fayoum 63514, Egypt

[3] The Institute of Optics, University of Rochester, Rochester, NY 14627, USA

other fiber amplifiers. The performance of all-optical NOT-OR (NOR) and exclusive-NOR (XNOR) logic gates has been investigated so far using SOAs at different speeds (Sharaiha et al. 2006; Kim et al. 2004, 2006a, b; Dong et al. 2008; Chen et al. 2016; Kotb et al. 2018a; Lee et al. 2002; Kang et al. 2009; Kotb and Maeda 2012). However, the SOAs infinite gain recovery time limits employing their operation at high speeds exceeded 100 Gb/s (Qin et al. 2016; Kumar and Shenoy 2014, 2016). On the other hand, placing quantum-dots (QDs) in the SOA active region is capable of bypassing the SOAs dynamics limitation to operate at higher speeds up to 2 Tb/s (Kotb et al. 2019a; Kotb and Guo 2019). In a QDSOA, the ultrafast gain recovery is achieved via the excited state carrier density, which acts as a carrier reservoir for the ground state (Kotb et al. 2019a; Kotb and Guo 2019). Therefore, the ultrafast gain recovery of the QDs in a scale of fs greatly improves the SOA nonlinearities response promising for optical signal processing applications, but their implementations in real applications are inherently difficult due to some practical issues. However, next-generation optical network systems will require advanced photonic devices to transfer higher repetition rates. A photonic crystal (PC), on the other hand, is a periodic optical nanostructure that uses to confine and control the light moves through its photonic energy gap (Baba 2008). The PC exhibits unique characteristics such as compact size, low absorption loss, low power consumption, high power transmission, high gain, and low noise over other nonlinear structures. These features make the PC a perfect candidate to enhance the SOA dynamics. In addition, the PCs have been successfully employed to enhance the performance of many optical devices, such as semiconductor lasers (Altug et al. 2006; Painter et al. 1999), all-optical switching (Nozaki et al. 2010), optical waveguides (Adibi et al. 2000), optical filter (Debnath et al. 2013), and (QD) SOAs (Mizuta et al. 2006; Cao et al. 2009; Nosratpour et al. 2018; Taleb and Abedi 2014; Kotb and Zoiros 2017; Kotb et al. 2018b, 2019b). Thus, in this paper, we continue and extend our previous relevant published work on PCSOAs technology (Kotb and Zoiros 2017; Kotb et al. 2018b; 2019b) by combining the PC features with those of conventional SOA to numerically model the performance of all-optical NOR and XNOR logic gates at 160 Gb/s. The configuration used to achieve this purpose is a Mach–Zehnder interferometer (MZI) where two symmetrical PCSOAs are embedded in its arms. The MZI combines many attractive and effective characteristics, such as sample structure, compact size, low-temperature dependence, the potential for ultrafast speed operation, reasonable energy requirement, and overall, practicality (Dutta and Wang 2013; Kotb 2012). In addition to that, a comparison has been made between PCSOAs and conventional SOAs devices through examining the variation of the quality factor (QF) against the schemes operational parameters, including the effects of the amplified spontaneous emission (ASE) and operating temperature ($T_{OP}$) in order to obtain more realistic results. The obtained results indicate that better logic performance and higher QF have been achieved only when using PCSOAs at 160 Gb/s compared to conventional SOAs.

The rest of this paper is organized as follows: the PCSOA model is detailed presented in Sect. 2. All-optical NOR and XNOR logic gates at 160 Gb/s are described in Sects. 3 and 4, respectively. Finally, Sect. 5 remarks on the obtained results.

## 2 PCSOA model

In this model, the PCSOA device consists of the GaInAsP core (active) layer with a refractive index of 3.45 and InP cladding layers with a refractive index of 3.17 (Nosratpour et al. 2018), as shown schematically in Fig. 1 (Kotb and Zoiros 2017; Kotb et al. 2018a,

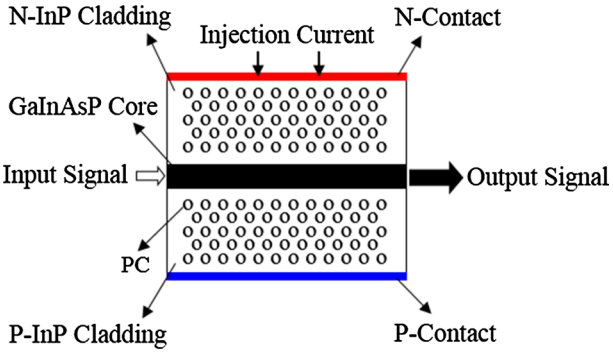


**Fig. 1** Schematic diagram of PCSOA waveguide

2019b). Deeply air holes, which allow a marked reduction in the device thermal resistance, are passing vertically through the whole SOA structure to form the PCs with a 0.158 µm radius, 2.3 µm depth, 0.480 µm lattice constant, and 0.42 µm spacing between rows (Kotb and Zoiros 2017; Kotb et al. 2018b, 2019). This PC waveguide is designed to operate around 1.55 µm optical communication wavelength. Fabrication of a PC waveguide integrated with a SOA is detailed presented in Ref. Cao et al. (2009).

The modulation format of the input pulse used in this model is a return-to-zero, which is widely used in network optical systems owing to its effective properties of better tolerance to fiber nonlinearity and improved receiver sensitivity (Breuer and Petermann 1997; Kawanishi 1998). The input pulse is assumed to be Gaussian-shaped having energy ($E_0$), full-width at half maximum (FWHM) pulse width ($\tau_{FWHM}$), and bit period (T), i.e. (Dutta and Wang 2013; Kotb 2012):

$$P_{A,B,Clk}(t) \equiv P_{in}(t) = \sum_{n=1}^{N} a_{n(A,B,Clk)} \frac{2\sqrt{\ln[2]}E_0}{\sqrt{\pi}\tau_{FWHM}} exp\left[-\frac{4\ln[2](t-NT)^2}{\tau_{FWHM}^2}\right] \quad (1)$$

where $\alpha_{n(A,B,Clk)}$ represents nth pulse, which takes the content binary '0' or '1' for A and B and '1' for clock signal (Clk) and $N = 2^7 - 1$ (Kotb and Zoiros 2017; Kotb et al. 2018b, 2019b) is the length of the pseudorandom binary sequence (PRBS).

By including the nonlinear interband as well as intraband effects, including carrier depletion (CD), carrier heating (CH), and spectral hole burning (SHB), the time-dependent gain of each PCSOA is then given by (Kotb and Zoiros 2017; Kotb et al. 2018b, 2019b):

$$\frac{dh_{CD}(t)}{dt} = \frac{h_0 - h_{CD}(t)}{\tau_C} - Rv_g h_{PC}(t) - \left(exp[h_{CD}(t) + h_{CH}(t) + h_{SHB}(t)] - 1\right)\frac{P_{in}(t)}{E_{sat}} \quad (2)$$

$$\frac{dh_{PC}(t)}{dt} = \frac{LR}{\tau_c}(h_0 - h_{PC}(t)) - Rv_g h_{CD}(t) \quad (3)$$

$$\frac{dh_{CH}(t)}{dt} = -\frac{h_{CH}(t)}{\tau_{CH}} - \frac{\varepsilon_{CH}}{\tau_{CH}}\left(\exp[h_{CD}(t) + h_{CH}(t) + h_{SHB}(t)] - 1\right)P_{in}(t) \quad (4)$$

$$\frac{dh_{SHB}(t)}{dt} = -\frac{h_{SHB}(t)}{\tau_{SHB}} - \frac{\varepsilon_{SHB}}{\tau_{SHB}}\left(\exp\left[h_{CD}(t) + h_{CH}(t) + h_{SHB}(t)\right] - 1\right)P_{in}(t) - \frac{dh_{CD}(t)}{dt} - \frac{dh_{CH}(t)}{dt} \tag{5}$$

where functions 'h' are the PCSOA gain integrated over its length due to CD ($h_{CD}$), PC ($h_{PC}$), CH ($h_{CH}$), and SHB ($h_{SHB}$). $h_0 = \ln[G_0]$, where $G_0$ is the unsaturated power gain, R is the radiation loss, and $v_g$ is the group velocity, which is linked to the group index ($n_g$) through $v_g = c/n_g$, where c is the light speed in space. The typical values of R and $n_g$ are, respectively, 30 $cm^{-1}$ and 3 for conventional SOAs while are 1500 $cm^{-1}$ and 100 for PCSOAs (Mizuta et al. 2006), resulting in a large gain even for a short length of PCSOA active region. $P_{in}(t)$ is the input pulse power, $E_{sat}$ is the saturation energy, which is linked to the saturation power ($P_{sat}$) by $E_{sat} = P_{sat}\ \tau_c$, where $\tau_c$ is the carrier lifetime. $\tau_{CH}$ is the temperature relaxation rate and $\tau_{SHB}$ is the carrier–carrier scattering rate. $\varepsilon_{CH}$ is the CH nonlinear gain suppression factor and $\varepsilon_{SHB}$ is the SHB nonlinear gain suppression factor. The time-dependent of each conventional SOA, taking into account interband and intraband effects are detailed described in Refs. Dutta and Wang (2013), Kotb (2012).

The total output gain of the amplifier, including PCSOA or bulk SOA, is given by Kotb and Zoiros (2017), Kotb et al. (2018, 2019b), Dutta and Wang (2013), Kotb (2012):

$$G_{(PC)SOA}(t) = \exp[h_{CD}(t) + h_{CH}(t) + h_{SHB}(t)] \tag{6}$$

While the phase change of the probe beam propagating through each (PC)SOA is given by Kotb and Zoiros (2017), Kotb et al. (2018, 2019b), Dutta and Wang (2013), Kotb (2012):

$$\Phi_{(PC)SOA}(t) = -0.5\left(\alpha h_{CD}(t) + \alpha_{CH} h_{CH}(t)\right) \tag{7}$$

where α is the traditional linewidth enhancement factor known as α-factor and $\alpha_{CH}$ is the CH linewidth enhancement factor. The contribution value of the SHB linewidth enhancement factor ($\alpha_{SHB}$) is null because the SHB is nearly asymmetrical around the input signal central wavelength and then the corresponding Kramers–Kronig integral will accordingly be antisymmetric and becomes very small (Kotb 2015a, b). The time-dependent gain equations of both PCSOA and SOA are prepared and run using Adam's numerical method in Mathematica Wolfram®. The more sensitive method to evaluate the performance quality is the QF, which is defined as the values of the mean peak powers of '1' bit and '0' bit divided by the sum of the corresponding noise standard deviations, i.e. $QF = (P_1 - P_0)/(\sigma_1 + \sigma_0)$ (Kotb and Zoiros 2017; Kotb et al. 2018b, 2019b; Dutta and Wang 2013; Kotb 2012). The QF value must be over six for the acceptable performance in order to keep the related bit-error-rate (Zhang and Dutta 2018; Kotb and Mohamed 2018; Thapa et al. 2019) less than $10^{-9}$ (Kotb and Zoiros 2017; Kotb et al. 2018b, 2019b). For a fair comparison, the operating parameters cited in Table 1 (Sharaiha et al. 2006; Kim et al. 2004, 2006a, b; Dong et al. 2008; Chen et al. 2016; Kotb et al. 2018b, 2018, 2019b; Lee et al. 2002; Kang et al. 2009; Kotb and Maeda 2012; Mizuta et al. 2006; Cao et al. 2009; Nosratpour et al. 2018; Taleb and Abedi 2014; Kotb and Zoiros 2017) have been used for both PCSOA and SOA structures. Notice, the parameter values used here are completely matching with the cited publications that have used similar physical and geometrical properties of PCSOAs and SOAs as those used in this simulation. In addition, most of these parameters are taken from experimental works (Mizuta et al. 2006; Cao et al. 2009; Dutta and Wang 2013).

**Table 1** Default parameters (Sharaiha et al. 2006; Kim et al. 2004, 2006, b; Dong et al. 2008; Chen et al. 2016; Kotb et al. 2018a; Lee et al. 2002; Kang et al. 2009; Kotb and Maeda 2012; Mizuta et al. 2006; Cao et al. 2009; Nosratpour et al. 2018; Taleb and Abedi 2014; Kotb and Zoiros 2017; Kotb et al. 2018b; Kotb et al. 2019b)

| Symbol | Definition | Value | Unit |
|---|---|---|---|
| $E_0$ | Pulse energy | 0.07 | pJ |
| $\tau_{FWHM}$ | Pulse width | 1 | ps |
| T | Bit period | 6.25 | ps |
| N | PRBS length | 127 | – |
| $\lambda_A$ | Wavelength of signal A | 1545 | nm |
| $\lambda_B$ | Wavelength of signal B | 1545 | nm |
| $\lambda_{Clk}$ | Wavelength of Clk | 1555 | nm |
| $\lambda_{CW}$ | Wavelength of CW | 1550 | nm |
| $P_A$ | Power of signal A | 2 | mW |
| $P_B$ | Power of signal B | 2 | mW |
| $P_{Clk}$ | Power of Clk | 2 | mW |
| $P_{CW}$ | Power of CW | 1 | mW |
| $P_{sat}$ | Saturation power | 10 | mW |
| I | Injection current | 10 | mA |
| $\tau_c$ | Carrier lifetime | 20 | ps |
| α | α-factor | 4 | – |
| $\alpha_{CH}$ | CH linewidth enhancement factor | 1 | – |
| $\alpha_{SHB}$ | SHB linewidth enhancement factor | 0 | – |
| $\varepsilon_{CH}$ | CH nonlinear gain suppression factor | 0.02 | $W^{-1}$ |
| $\varepsilon_{SHB}$ | SHB nonlinear gain suppression factor | 0.02 | $W^{-1}$ |
| $\tau_{CH}$ | Temperature relaxation rate | 0.3 | ps |
| $\tau_{SHB}$ | Carrier–carrier scattering rate | 0.1 | ps |
| Γ | Confinement factor | 0.15 | – |
| a | Differential gain | $2\times10^{-16}$ | $cm^{-3}$ |
| L | Length of active layer | 10 | μm |
| d | Thickness of active layer | 0.3 | μm |
| w | Width of active region | 3 | μm |
| $N_{SP}$ | Spontaneous emission factor | 2 | – |
| $G_0$ | Unsaturated power gain | 1000 | – |
| $B_0$ | Optical bandwidth | 2 | GHz |
| υ | Optical frequency | 193.55 | THz |
| $T_{op}$ | Operating temperature | 290 | K |

## 3 All-optical NOR logic gate at 160 Gb/s

A NOR gate is logically an inverted OR gate that gives 'on' output only when both inputs are 'off'. The other logic gates can be generated by a combination of NOR gates, which are so-called 'universal gates'. A schematic diagram and truth table of the NOR gate using PCSOAs-based MZI are shown in Fig. 2.

As shown in Fig. 2, the input powers injected into PCSOA1 and PCSOA2 are, respectively, formulated by:

$$P_{in,PCSOA_1}(t) = P_A(t) + P_B(t) + 0.5\,P_{CW} \tag{8}$$

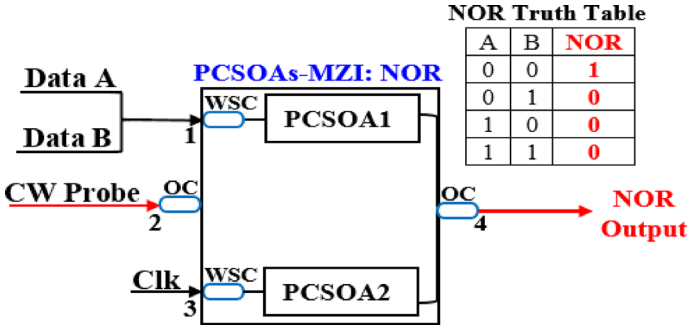


**Fig. 2** Schematic diagram and truth table of NOR gate using PCSOAs-MZI. OC: 3 dB optical coupler. WSC: wavelength selective coupler

$$P_{in,PCSOA_2}(t) = P_{Clk}(t) + 0.5\,P_{CW} \tag{9}$$

where the coefficient '0.5' refers to the halving of the CW beam via 3 dB OC.

The NOR output power coming out of PCSOAs-MZI at port 4 is then given by Dutta and Wang (2013), Kotb (2015a):

$$P_{out,\,NOR}(t) = 0.25\,P_{CW}\left(G_{PCSOA_1}(t) + G_{PCSOA_2}(t) - 2\sqrt{G_{PCSOA_1}(t)\,G_{PCSOA_2}(t)}\cos\left[\Phi_{PCSOA_1}(t) - \Phi_{PCSOA_2}(t)\right]\right) \tag{10}$$

In order to realize the NOR operation using PCSOAs-MZI, data signal A is combined with data signal B using a wavelength selective coupler (WSC) to enter PCSOA1 from port 1 as ($P_A + P_B$), while the Clk is inserted into PCSOA2 from port 3. The main role of using WSCs is to couple the input pump signals (A, B, and Clk) to PCSOAs while rejecting out all other unwanted wavelengths. These signals modulate the device gain and thereby the phase of the continues-wave (CW), which is split by a 3 dB optical coupler (OC) into two equal intensity outputs to inject into both PCSOA1 and PCSOA2 through the PCSOAs-MZI middle arm at port 2. When signals A and B combination (10, 01, or 11) and the Clk (all 1's) are launched into PCSOA1 and PCSOA2, respectively, PCSOAs-MZI get saturated quickly, therefore, the modulated CW phases passing through both PCSOA1 and PCSOA2 will be equal, resulting in '0' output from port 4 due to the destructive interference. When signals A and B combination (00) and the Clk (all 1's) are inserted into PCSOA1 and PCSOA2, respectively, the modulated CW probe beam will be interfered constructively to result in '1' logic output. This means that the PCSOAs-MZI binary output is '1' only when both signals A and B are '0', which is functionally the NOR gate according to its inset truth table shown in Fig. 2.

The numerical results of the output traces and eye diagram for the NOR gate for the input signals A and B using PCSOAs- and conventional SOAs-based MZI at 160 Gb/s are, respectively, shown in Figs. 3 and 4. There are no pulse amplitude fluctuations and the eye diagram is open and clear with 20.1 QF using PCSOAs, while much amplitude fluctuations with unacceptable QF (i.e. 3.42) are obtained when using conventional SOAs. This happened because of enhanced light-matter interaction in PC cavity leads to an enhancement of the nonlinearities effects, resulting in higher QF (Bakoz et al. 2018).

Low QF value is an expected result of high input power, while high injection current is necessary to achieve high QF value for both PCSOAs and conventional SOAs. More

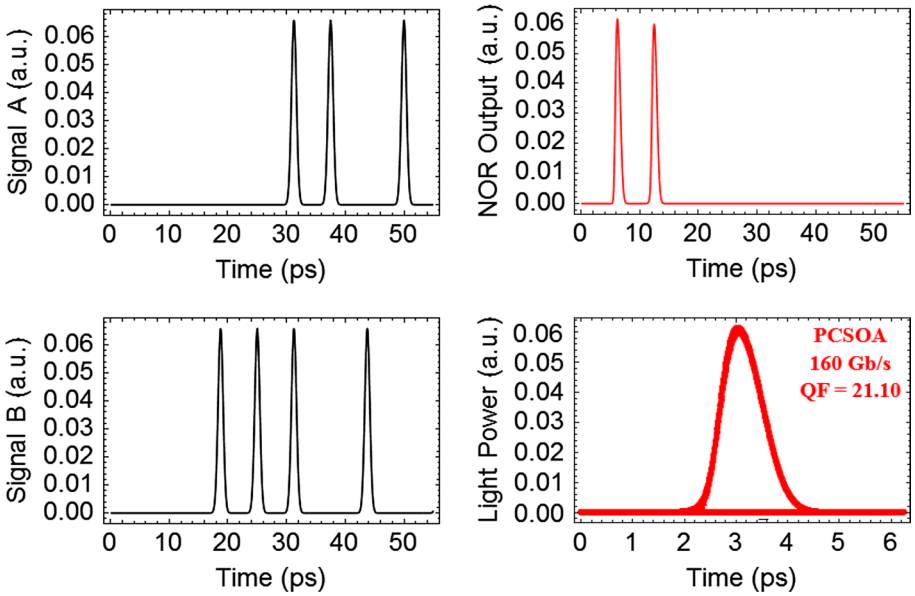


**Fig. 3** NOR numerical results using PCSOAs-MZI at 160 Gb/s

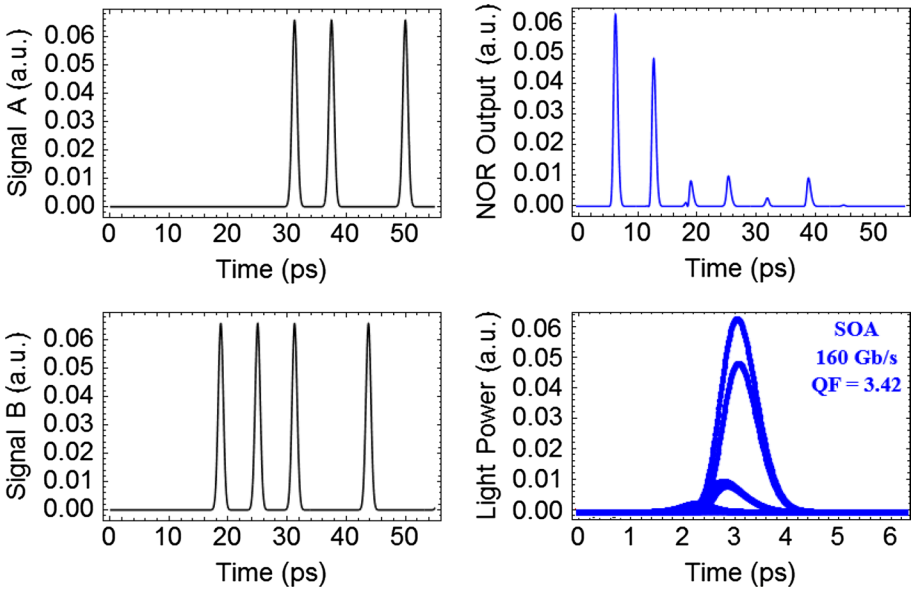


**Fig. 4** NOR numerical results using conventional SOAs-MZI at 160 Gb/s

clarification, high input data A, B peak power depletes the carriers in the amplifier active region via the stimulated emission process that, in turn, causes a degradation in QF, which remains a more acceptable value up to 9 mW when using PCSOAs, as seen in Fig. 5a.

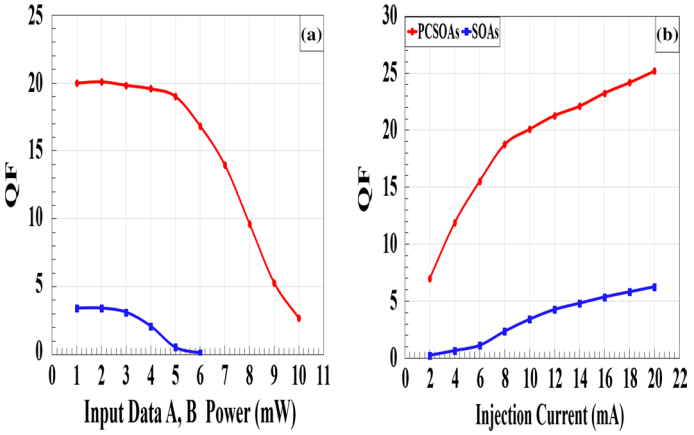


**Fig. 5** NOR QF versus **a** input data A, B power and **b** injection current using PCSOAs- and conventional SOAs-based MZI at 160 Gb/s

On the other hand, the optical gain is physically produced by the radiative recombination of electrons and holes injected by the external forward bias current. Since the number of carrier densities increases with supplying more external current inside the amplifier, this, in turn, enhances the amplifier dynamics at constant temperature and hence increases the output QF, as shown in Fig. 5b. The amount of injection current required to achieve acceptable QF using PCSOAs is ten times smaller than for conventional SOAs. These figures indicate that the performance of all-optical NOR gate using PCSOAs is more acceptable even at high input power or low injection current.

The traditional linewidth enhancement factor (α-factor) is a powerful parameter for designing SOA devices. In SOA, the α-factor is defined as the ratio of the changes of the refractive index (n) and the net gain (g) with a change in the carrier density (N) linearly through the following equation (Wang et al. 2007):

$$\alpha = -\frac{4\pi}{\lambda}\frac{(dn/dN)}{(dg/dN)} \tag{11}$$

The α-factor can be obtained in practice by relating the total phase change with the total gain change of the signal passing through the device length as formulated in Eq. (7). The α-factor has been measured experimentally using a pump-probe experiment in SOAs (Wang et al. 2007). The integrated gain response and the phase shift are much more efficient in PCSOAs than in conventional SOAs leads to enhance the performance of the NOR operation even at small α-factor, as shown in Fig. 6a. In addition, the α-factor increases with an increase in both injection current and active region length (Occhi et al. 2001) and these two later key parameters cause a generous increase in QF value, especially when using PCSOA structure (Kotb and Zoiros 2017; Kotb et al. 2018b, 2019b). On the right side, similar behavior is seen in Fig. 6b where the QF versus the optical confinement factor (Γ) for both amplifiers. Γ is defined as the ratio of the average energy density in the device active layer to the average energy density in the device waveguide (Connelly 2002). Less average energy density is confined into the active layer at low Γ that affects the saturation level of the SOA device, resulting in low QF, which is more acceptable when using PCSOA structure.

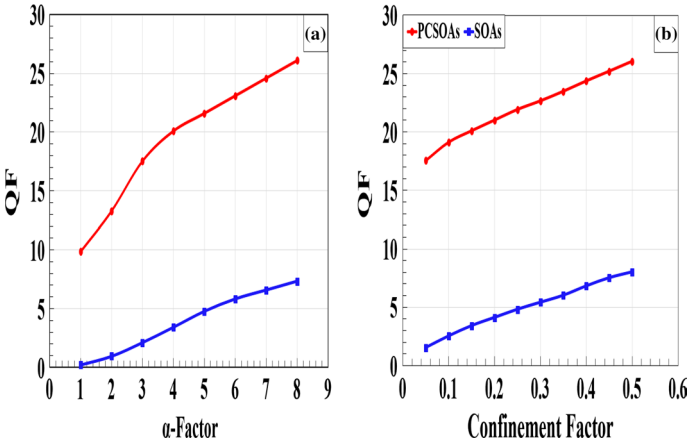


**Fig. 6** NOR QF versus **a** traditional linewidth enhancement factor (α-factor) and **b** confinement factor using PCSOAs- and conventional SOAs-based MZI at 160 Gb/s

To get further insight into the NOR performance, Fig. 7 compares the graphs of the NOR QF versus the operating data rate and equivalent PRBS length at 160 Gb/s using PCSOAs and conventional SOAs. The operating data rate is the number of bits per second that can be transferred through the waveguide. The QF decreases with increasing the operating data rate for both devices, as shown in Fig. 7a, but its value (~ 7.12) is more acceptable when using PCSOAs even up to 320 Gb/s, while this is impossible to be achieved when using conventional SOAs owing to their slower dynamics response. Despite the PRBS has a negative effect on both devices, but the PCSOA scheme is tolerant of this effect and its QF is more acceptable across the whole scanned range of PRBS, as shown in Fig. 7b. These results confirm that the PCSOAs are excellent candidates in applications that required high data rates and high PRBS length with more acceptable performance than conventional SOAs.

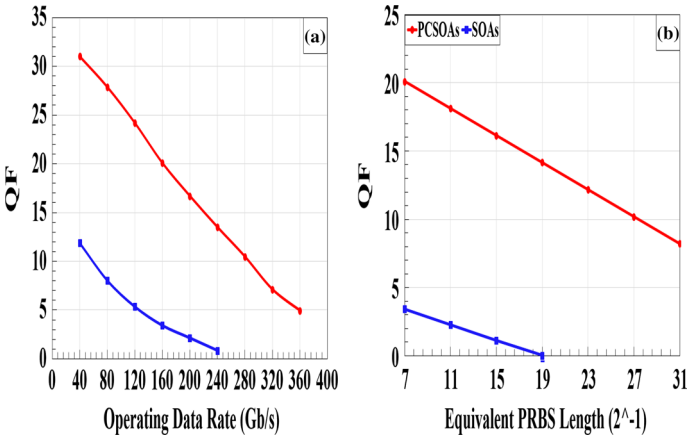


**Fig. 7** NOR QF versus **a** operating data rate and **b** equivalent pseudorandom binary sequence (PRBS) length using PCSOAs- and conventional SOAs-based MZI at 160 Gb/s

This modeling includes the effects of the amplified spontaneous emission (ASE) and operating temperature in order to obtain more realistic results. The ASE power is defined as $P_{ASE} = N_{SP}(G_0 - 1)2\pi\hbar\upsilon B_0$(Dutta and Wang 2013; Kotb 2012; Connelly 2002), where $N_{sp}$ is the spontaneous emission factor, which is equal '2' for an ideal amplifier (Kotb et al. 2011), ħ is the reduced Planck's constant, and $B_0$ is the optical bandwidth at an optical frequency υ. The values of these parameters are cited in Table 1. The ASE power is numerically added using the above expression to the NOR output power given in Eq. (10). Large ASE power increases the average intensity of pulse '0', resulting in a QF degradation for both devices, as shown in Fig. 8a. It can be clearly observed that the QF using PCSOAs is not highly affected by the ASE noise and is still having more acceptable QF than SOAs even at high values of ASE power. On the other hand, improving SOA performance to operate at high temperature is a very important area of investigation. The probability of carriers occupation in the device active region increases at low operating temperature ($T_{OP}$). As shown in Fig. 8b, the QF is decreased as the temperature becomes higher. This happens because the electrons are distributed over a wider energy range at high temperature and therefore the number of electrons, which are available for participating in device gain, became fewer. The nonradiative recombination increases with temperature, resulting in a reduction in device gain. The SOA transparency point can also be changed by the temperature, and hence affect the SOA gain recovery time. In fact, high operating temperature causes an increase in the amplifier carrier lifetime and a reduction in its peak gain (Kumar and Shenoy 2016). It should be noted that the PCSOA runs effectively without an active cooling unit and the sole purpose of Fig. 8b is to compare the characteristics of both devices at varying $T_{OP}$. These figures show that the QF using PCSOAs is slowly decreased with ASE power and $T_{OP}$, while the QF is fast dropped when using SOAs. Overall, the PCSOAs provide better performance than SOAs even at higher ASE power and higher $T_{OP}$.

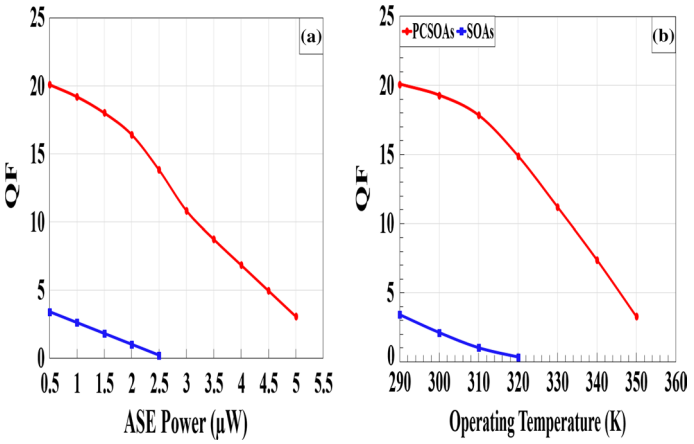


**Fig. 8** NOR QF versus **a** amplified spontaneous emission (ASE) power and **b** operating temperature using PCSOAs- and conventional SOAs-based MZI at 160 Gb/s

## 4 All-optical XNOR logic gate at 160 Gb/s

The output of the XNOR gate is '1' only when the inputs have the same value, i.e. '0' or '1'. This means that the XNOR gate is a XOR gate followed by an invert operation (Shaik and Rangaswamy 2018). The schematic diagram and truth table of the XNOR gate formed by a series combination of XOR and invert operations using PCSOAs-based MZIs are shown in Fig. 9.

The input powers going inside PCSOA1 and PCSOA2 of the PCSOAs-MZI1 in order to realize first the XOR operation are, respectively, described by (Dutta and Wang 2013; Kotb 2012):

$$P_{in,PCSOA_1}(t) = P_A(t) + 0.5\,P_{CW} \tag{12}$$

$$P_{in,PCSOA_2}(t) = P_B(t) + 0.5\,P_{CW} \tag{13}$$

The output power of the XOR gate of PCSOAs-MZI1 is then given by (Kotb and Zoiros 2017; Kotb et al. 2011):

$$P_{XOR,MZI1}(t) = 0.25\,P_{CW}\left(G_{PCSOA_1}(t) + G_{PCSOA_2}(t) - 2\sqrt{G_{PCSOA_1}(t)\,G_{PCSOA_2}(t)}\,cos\left[\Phi_{PCSOA_1}(t) - \Phi_{PCSOA_2}(t)\right]\right) \tag{14}$$

While the input powers going into PCSOA3 and PCSOA4 of the PCSOAs-MZI2 for the Invert operation are, respectively, described by Kotb (2015b):

$$P_{in,PCSOA_3}(t) = P_{XOR,MZI1}(t) + 0.5\,P_{CW} \tag{15}$$

$$P_{in,PCSOA_4}(t) = P_{Clk}(t) + 0.5\,P_{CW} \tag{16}$$

where the coefficient '0.5' refers to the halving of CW light via 3 dB OC.

Therefore, the XNOR output power coming out of PCSOAs-MZIs at port 8 is given by (Kotb 2012, 2015b):

$$P_{XNOR,MZI2}(t) = 0.25\,P_{CW}\left(G_{PCSOA_3}(t) + G_{PCSOA_4}(t) - 2\sqrt{G_{PCSOA_3}(t)\,G_{PCSOA_4}(t)}\,cos\left[\Phi_{PCSOA_3}(t) - \Phi_{PCSOA_4}(t)\right]\right) \tag{17}$$

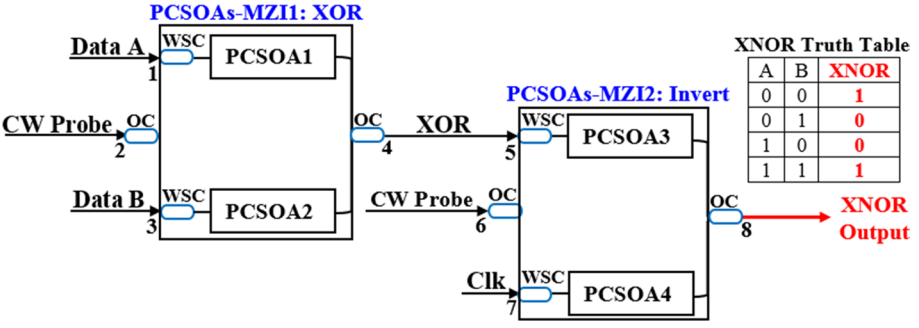


**Fig. 9** Schematic diagram and truth table of XNOR gate using PCSOAs-based MZIs. OC: 3 dB optical coupler. WSC: wavelength selective coupler

In order to realize the XOR operation using PCSOAs-MZI1, a CW probe beam is split equally by 3 dB OC and injected into the middle arm of PCSOAs-MZI1. Using WSCs, half of CW is combined with data A injected from port1 into PCSOA1, while the other half of CW is combined with data B injected into PCSOA2 from port 3. Pump signals A and B perturb PCSOAs-MZI1 arms dynamics and change the CW phase on which the switching outcome is transferred at the PCSOAs-MZI1 output. Logically, When both A and B are the same, i.e. '0' or '1', the PCSOAs-MZI1 remains balanced and thus there is no phase change on CW constituents, which interfere destructively when they recombined by OC located at port 4 and so the structure output remains at low amplitude level, i.e. '0'. While when signals A and B differs, i.e. A = '0' and B = '1' or A = '1' and B = '0', the MZI dynamic symmetry is broken and there is phase change on CW constituents, which is translated into amplitude modulation of high level, i.e. '1', due to constructive interference at the structure output. In this manner, the XOR operation is executed between signals A and B. This output XOR gate and a Clk signal (all 1's) are combined via WSCs with CW beam injected into the PCSOAs-MZI2 middle arm and then guided into PCSOA3 and PCSOA4, respectively, in order to realize the XNOR operation. In this way, the XNOR outcome between A and B is obtained from PCSOAs-MZI2 output.

The output numerical results for the XNOR gate using PCSOAs- and conventional SOAs-based MZIs at 160 Gb/s are depicted in Figs. 10 and 11, respectively. Using PCSOAs structure achieves higher QF than conventional SOAs, i.e. 15.83 versus 3.38.

The XNOR QF variation against the input data A, B power and injection current using PCSOAs- and conventional SOAs-based MZIs at 160 Gb/s is shown in Fig. 12. Still, the QF using PCSOAs is more acceptable through the whole scan than conventional SOAs.

The dependence of the XNOR QF on the α-factor and confinement factor (Γ) using PCSOAs- and conventional SOAs-based MZIs at 160 Gb/s is shown in Fig. 13. Higher QF is obtained even at low values of α-factor and Γ when using only PCSOAs.

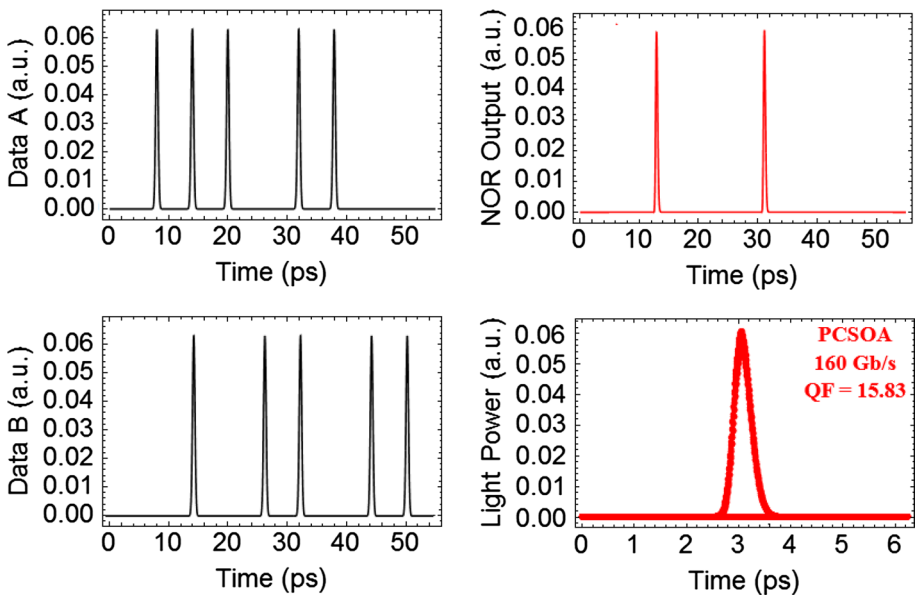


**Fig. 10** XNOR numerical results using PCSOAs-MZIs at 160 Gb/s

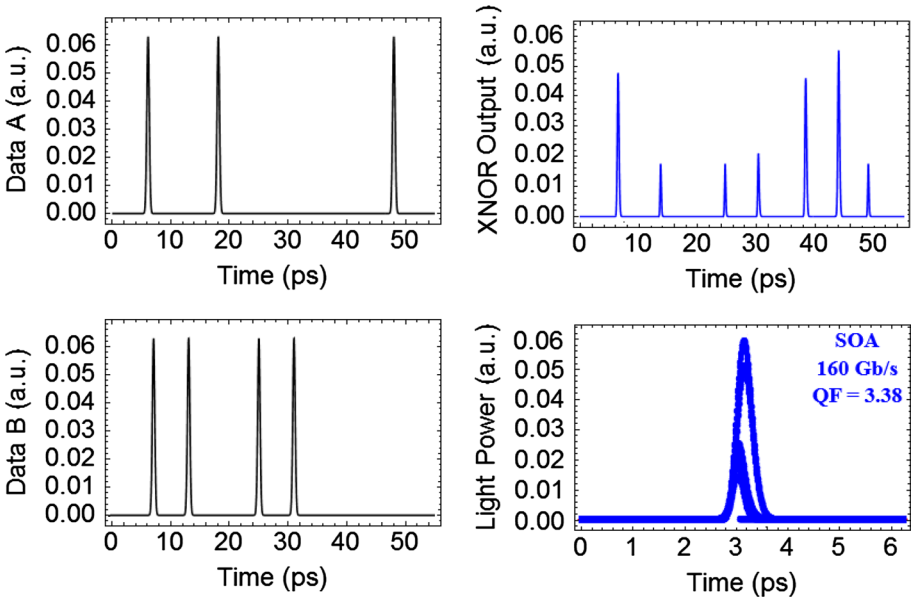


**Fig. 11** XNOR numerical results using conventional SOAs-MZIs at 160 Gb/s

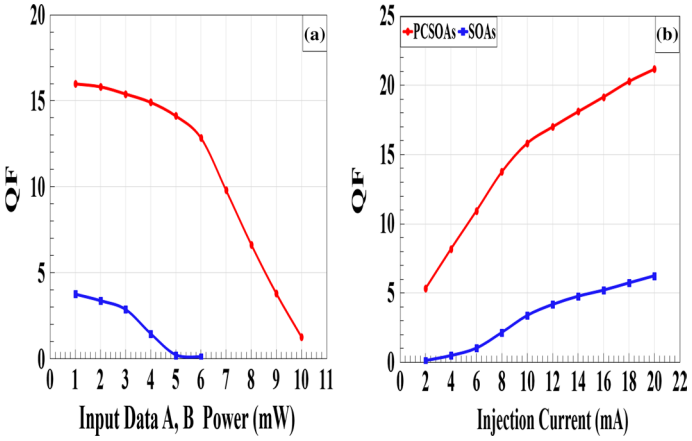


**Fig. 12** XNOR QF versus **a** input data A, B power and **b** injection current using PCSOAs- and conventional SOAs-based MZIs at 160 Gb/s

The XNOR QF versus the operating data rate and equivalent PRBS length using PCSOAs- and conventional SOAs-based MZIs at 160 Gb/s is shown in Fig. 14. The PCSOAs-based XNOR can be operated up to 280 Gb/s with 6.63 QF and that's is impossible to be achieved using conventional SOAs.

Figure 15 shows the QF versus the ASE power and operating temperature using PCSOAs- and conventional SOAs-based MZIs at 160 Gb/s. It can be clearly seen that

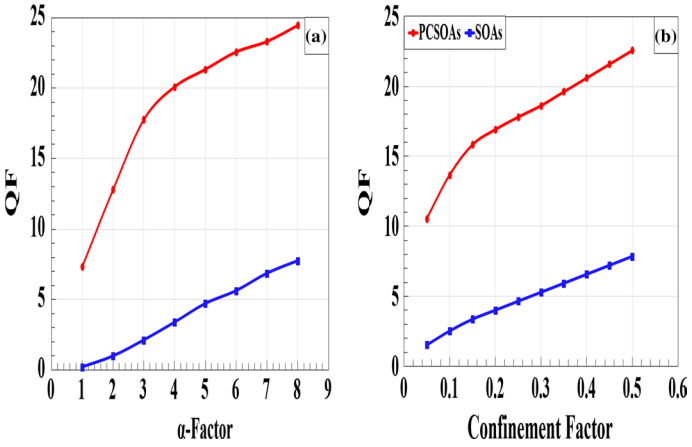


**Fig. 13** XNOR QF versus **a** α-factor and **b** confinement factor using PCSOAs- and conventional SOAs-based MZIs at 160 Gb/s

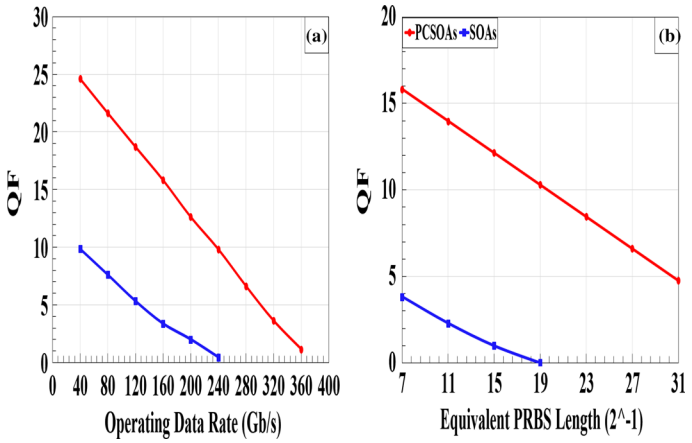


**Fig. 14** XNOR QF versus **a** operating data rate and **b** equivalent PRBS length using PCSOAs- and conventional SOAs-based MZIs at 160 Gb/s

the PCSOAs effectively operate at higher ASE and higher temperatures with better performance compared to conventional SOAs.

The SOAs integrated PC waveguide being used in this simulation are commercial cheap grade devices. Therefore, the cost of the employed scheme used to realize all-optical NOR and XNOR logic gates is affordable and justified by doubling the operating data rate (160 Gb/s) with much higher QF compared to SOAs used for the same purpose. In addition to that, the input data power required to achieve these amazing results does not exceed 2 mW, which can be easily practically supplied by using a conventional erbium-doped fiber amplifier.

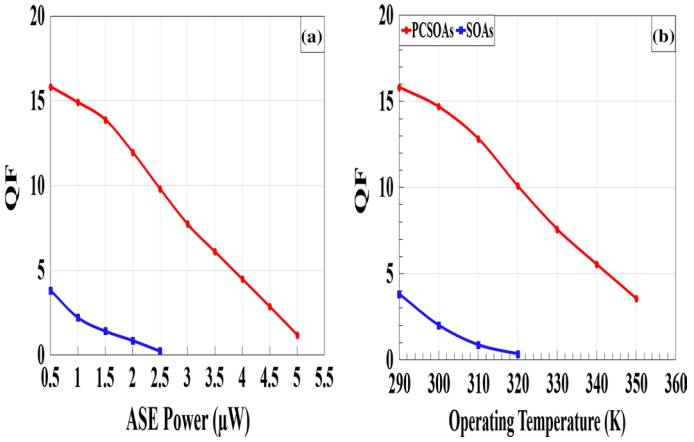


**Fig. 15** XNOR QF versus **a** ASE power and **b** operating temperature using PCSOAs- and conventional SOAs-based MZIs at 160 Gb/s

## 5 Conclusion

In this paper, the operation of ultrafast all-optical NOR and XNOR logic gates was numerically modeled at 160 Gb/s using photonic crystal semiconductor optical amplifiers (PCSOAs)-based Mach–Zehnder interferometer. The variation of the gates' quality factor (QF) against the operational key parameters was examined, including the effects of the ASE and operating temperature in order to obtain more realistic outcomes. Compared to conventional SOAs, the results overall confirmed that the considered Boolean functions can be implemented using PCSOAs with more than acceptable performance.

**Acknowledgements** This work was funded by the Chinese Academy of Sciences President's International Fellowship Initiative (Grant No. 2019FYT0002) and Talented Young Scientist Program supported by the China Science and Technology Exchange Center of Ministry of Science and Technology of China.

## References

Adibi, A., Lee, R., Xu, Y., Yariv, A., Scherer, A.: Design of photonic crystal optical waveguide with single-mode propagation in the photonic bandgap. Electron. Lett. **36**, 1376–1378 (2000)

Altug, H., Englund, D., Vučković, J.: Ultrafast photonic crystal nanocavity laser. Nat. Phys. **2**, 484–488 (2006)

Baba, T.: Slow light in photonic crystal. Nat. Photonics **2**, 465–473 (2008)

Bakoz, A.P., Liles, A.A., Gonzalez-Fernandez, A.A., Habruseva, T., Hu, C., Viktorov, E.A., Hegarty, S.P., O'Faolain, L.: Wavelength stability in a hybrid photonic crystal laser through controlled nonlinear absorptive heating in the reflector. Light Sci. Appl. **7**, 438–444 (2018)

Breuer, D., Petermann, K.: Comparison of NRZ- and RZ-modulation format for 40-Gb/s TDM standard-fiber systems. IEEE Photonics Technol. Lett. **9**, 398–400 (1997)

Cao, T., Ho, Y.L.D., Heard, P.J., Barry, L.P., Kelly, A.E., Cryan, M.J.: Fabrication and measurement of a photonic crystal waveguide integrated with a semiconductor optical amplifier. J. Opt. Soc. Am. B **26**, 768–777 (2009)

Chen, X., Huo, L., Zhao, Z., Zhuang, L., Lou, C.: Study on 100-Gb/s reconfigurable all-optical logic gates using a single semiconductor optical amplifier. Opt. Express **24**, 30245–30253 (2016)

Connelly, M.J.: Semiconductor Optical Amplifiers. Springer, New York (2002)
Debnath, K., Welna, K., Ferrera, M., Deasy, K., Lidzey, D.G., O'Faolain, L.: Highly efficient optical filter based on vertically coupled photonic crystal cavity and bus waveguide. Opt. Lett. **38**, 154–156 (2013)
Dong, J., Zhang, X., Xu, J., Huang, D.: 40 Gb/s all-optical logic NOR and OR gates using a semiconductor optical amplifier: experimental demonstration and theoretical analysis. Opt. Commun. **281**, 1710–1715 (2008)
Dutta, N.K., Wang, Q.: Semiconductor Optical Amplifiers, 2nd edn. World Scientific Publishing Company, Singapore (2013)
Kang, I., Rasras, M., Buhl, L., Dinu, M., Cabot, S., Cappuzzo, M., Gomez, L.T., Chen, Y.F., Patel, S.S., Dutta, N.K., Piccirilli, A., Jaques, J., Giles, C.R.: All-optical XOR and XNOR operations at 86.4 Gb/s using a pair of semiconductor optical amplifier Mach–Zehnder interferometers. Opt. Express **17**, 19062–19065 (2009)
Kawanishi, S.: Ultrahigh-speed optical time-division-multiplexed transmission technology based on optical signal processing. IEEE J. Quantum Electron. **34**, 2064–2079 (1998)
Kim, J.H., Kim, Y.I., Byun, Y.T., Jhon, Y.M., Lee, S., Kim, S.H., Woo, D.H.: All-optical logic gates using semiconductor optical-amplifier-based devices and their applications. J. Korean Phys. Soc. **45**, 1158–1161 (2004)
Kim, J.Y., Kang, J.M., Kim, T.Y., Han, S.K.: All-optical multiple logic gates with XOR, NOR, OR and NAND function using parallel SOA-MZI structures: theory and experiment. J. Lightwave Technol. **24**, 3392–3399 (2006a)
Kim, J.Y., Kang, J.M., Kim, T.Y., Han, S.K.: 10 Gbits all-optical composite logic gates with XOR, NOR, OR and NAND functions using SOA-MZI structures. Electron. Lett. **42**, 303–307 (2006b)
Kotb, A.: All-Optical Logic Gates Using Semiconductor Optical Amplifier. Lambert Academic Publishing, Saarbrucken (2012)
Kotb, A.: Simulation of all-optical logic NOR gate based on two-photon absorption with semiconductor optical amplifier-assisted Mach–Zehnder interferometer with the effect of amplified spontaneous emission. J. Korean Phys. Soc. **66**, 1593–1598 (2015a)
Kotb, A.: Modeling of high-quality-factor XNOR gate using quantum-dot semiconductor optical amplifiers at 1 Tb/s. Braz. J. Phys. **45**, 288–295 (2015b)
Kotb, A., Guo, C.: Two-photon absorption in quantum dot semiconductor optical amplifiers-based all-optical XOR gate at 2 Tb/s. Opt. Quantum Electron. **51**(58), 1–12 (2019)
Kotb, A., Maeda, J.: All-optical logic NXOR based on semiconductor optical amplifiers with the effect of amplified spontaneous emission. Optoelectron. Lett. **8**, 437–440 (2012)
Kotb, A., Mohamed, Y.: Phase-shift keying modulated data signal using SOA-MZI-based all-optical logic AND gate at 80 Gb/s. Int. J. Opt. **2018**(5864530), 1–8 (2018)
Kotb, A., Zoiros, K.E.: Performance analysis of all-optical XOR gate with photonic crystal semiconductor optical amplifier-assisted Mach–Zehnder interferometer at 160 Gb/s. Opt. Commun. **402**, 511–517 (2017)
Kotb, A., Ma, S., Chen, Z., Dutta, N.K., Said, G.: Effect of amplified spontaneous emission on semiconductor optical amplifier based all-optical logic. Opt. Commun. **284**, 5798–5803 (2011)
Kotb, A., Zoiros, K.E., Guo, C.: All-optical XOR, NOR, and NAND logic functions with parallel semiconductor optical amplifier-based Mach–Zehnder interferometer modules. Opt. Laser Technol. **108**, 426–433 (2018a)
Kotb, A., Zoiros, K.E., Guo, C.: 160 Gb/s photonic crystal semiconductor optical amplifiers-based all-optical logic NAND gate. Photon Netw. Commun. **36**, 246–255 (2018b)
Kotb, A., Zoiros, K.E., Guo, C.: 2 Tb/s all-optical gates based on two-photon absorption in quantum dot semiconductor optical amplifiers. Opt. Laser Technol. **112**, 442–451 (2019a)
Kotb, A., Zoiros, K.E., Guo, C.: Ultrafast performance of all-optical AND and OR logic operations at 160 Gb/s using photonic crystal semiconductor optical amplifier. Opt. Laser Technol. **119**(105611), 1–10 (2019b)
Kumar, Y., Shenoy, M.R.: A novel scheme of optical injection for fast gain recovery in semiconductor optical amplifier. IEEE Photonics Technol. Lett. **26**, 933–936 (2014)
Kumar, Y., Shenoy, M.R.: Enhancement in the gain recovery of a semiconductor optical amplifier by device temperature control. Pramana J. Phys. **87**, 1–6 (2016)
Lee, S., Park, J., Lee, K., Eom, D., Lee, S., Kim, J.H.: All-optical exclusive NOR logic gate using Mach–Zehnder interferometer. Jpn. J. Appl. Phys. **41**, 1155–1157 (2002)
Mizuta, E., Watanabe, H., Baba, T.: All semiconductor low-$\Delta$ photonic crystal waveguide for semiconductor optical amplifier. Jpn. J. Appl. Phys. **45**, 6116–6120 (2006)
Nosratpour, A., Razaghi, M., Darvish, G.: Computational study of pulse propagation in photonic crystal semiconductor optical amplifier. J. Nanophotonics **12**(036015), 1–12 (2018)

Nozaki, K., Tanabe, T., Shinya, A., Matsuo, S., Sato, T., Taniyama, H., Notomi, M.: Sub-femtojoule all-optical switching using a photonic-crystal nanocavity. Nat. Photonics **4**, 477–483 (2010)
Occhi, L., Scollo, R., Schares, L., Guekos, G.: Effective alpha factor in bulk semiconductor optical amplifiers of different lengths. In: 14th Annual Meeting of the IEEE Lasers and Electro-Optics Society, vol. 1, pp. 105–106 (2001)
Painter, O., Lee, R.K., Scherer, A., Yariv, A., O'Brien, J.D., Dapkus, P.D., Kim, I.: Two-dimensional photonic bandgap defect mode laser. Science **284**, 1819–1821 (1999)
Qin, C., Zhao, J., Yu, H., Zhang, J.: Gain recovery dynamics in semiconductor optical amplifiers with distributed feedback grating under assist light injection. Opt. Eng. **55**(076116), 1–7 (2016)
Shaik, E.H., Rangaswamy, N.: Realization of XNOR logic function with all-optical high contrast XOR and NOT gates. Opto Electron. Rev. **26**, 63–72 (2018)
Sharaiha, A., Topomondzo, J., Morel, P.: All-optical logic AND-NOR gates with three inputs based on cross-gain modulation in a semiconductor optical amplifier. Opt. Commun. **265**, 322–325 (2006)
Taleb, H., Abedi, K.: Design of a novel low power all-optical NOR gate using photonic crystal quantum-dot semiconductor optical amplifiers. Opt. Lett. **39**, 6237–6241 (2014)
Thapa, S., Zhang, X., Dutta, N.K.: Effects of two-photon absorption on pseudo-random bit sequence operating at high speed. J. Mod. Opt. **66**, 100–108 (2019)
Wang, J., Maitra, A., Poulton, C.G., Freude, W., Leuthold, J.: Temporal dynamics of the alpha factor in semiconductor optical amplifiers. J. Lightwave Technol. **25**, 891–900 (2007)
Zhang, X., Dutta, N.K.: Effects of two-photon absorption on all-optical logic operation based on quantum-dot semiconductor optical amplifiers. J. Mod. Opt. **65**, 166–173 (2018)